Received: 31 October 2019 | Revised: 28 November 2019 | Accepted: 8 December 2019

DOI: 10.1002/ppap.201900217

PLASMA PROCESSES AND POLYMERS

FULL PAPER

Turbulence and entrainment in an atmospheric pressure dielectric barrier plasma jet

Youssef Morabit[1] | Richard D. Whalley[2] | Eric Robert[3] | Mohammad I. Hasan[1] | James L. Walsh[1]

[1]Department of Electrical Engineering and Electronics, Centre for Plasma Microbiology, University of Liverpool, Liverpool, UK

[2]School of Engineering, Newcastle University, Newcastle upon Tyne, UK

[3]GREMI, CNRS Université d'Orléans, UMR 7344, Orléans, France

Correspondence
James L. Walsh, Department of Electrical Engineering and Electronics, Centre for Plasma Microbiology, University of Liverpool, L69 3GJ, Liverpool, UK.
Email: jlwalsh@liverpool.ac.uk

Funding information
Engineering and Physical Sciences Research Council,
Grant/Award Numbers: EP/N021347/1, EP/R041849/1, EP/S017623/1, EP/S025790/1

Abstract

Particle image velocimetry, laser-induced fluorescence, and computational modeling are used to quantify the impact of plasma generation on air entrainment into a helium plasma jet. It is demonstrated that discharge generation yields a minor increase in the exit velocity of the gas. In contrast, the laminar to turbulent transition point is strongly affected, attributed to an increase in plasma-induced perturbations within the jet shear layer. The temporal decay of laser-induced fluorescence from OH is used as an indicator of humid air within the plasma. The results show that plasma-induced perturbations increase the quenching rate of the OH-fluorescent state; indicating that shear-layer instabilities play a major role in determining the physicochemical characteristics of the plasma.

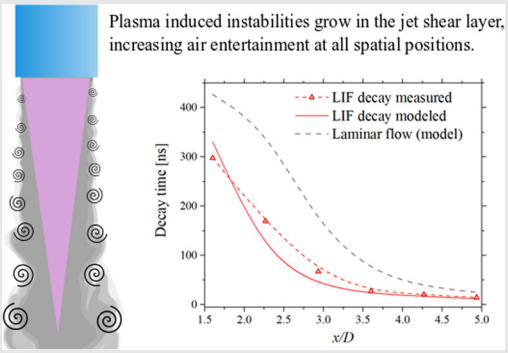

KEYWORDS
LIF, PIV, plasma, turbulence

1 | INTRODUCTION

Atmospheric pressure plasma jets have been widely used in many healthcare and materials processing applications, ranging from etching and deposition to microbial decontamination and cancer therapy.[1–5] Perhaps the most widely used plasma jet configuration is based on the dielectric barrier discharge employing a noble gas such as helium or argon; typically, the gas is flushed through a dielectric capillary and subjected to an applied voltage using one or more electrodes placed inside and/or outside of the capillary. On the application of a time-varying voltage of sufficient magnitude to cause a breakdown, a discharge forms within the capillary and propagates as a fast-moving ionization wave along the noble gas channel, ultimately exiting the capillary and extending into the surrounding quiescent air. From an application perspective, atmospheric pressure plasma-based applications typically rely on reactive oxygen and nitrogen species (RONS), many of which are created through the interaction between the plasma plume and the quiescent air.

A large number of studies have considered the impact that the plasma generation has on the characteristics of

the flowing noble gas. It has been widely reported that the generation of plasma in a buoyant axisymmetric jet configuration leads to a rapid transition from laminar to turbulent flow.[6–10] It is commonly assumed that gas heating and electrohydrodynamic (EHD) forces play a role in creating turbulence within the flowing gas channel, with the latter being considered as the dominant mechanism. Indeed, Park et al.[11] used a pulsed plasma jet to demonstrate that EHD forces are primarily exerted by space charge drifting in the applied electric field following streamer propagation, confirming the modeling results of Hasan and Bradley.[12] Whalley and Walsh demonstrated that the spatially developing velocity fields in an inhomogeneous axisymmetric plasma jet flow are turbulent and self-similar, with characteristics matching the turbulent velocity fields which develop naturally with increasing distance from the jet exit.[8] Using an order-of-magnitude analysis, it was predicted that the presence of a discharge should only increase the jet exit velocity by approximately 10%. Many studies in the field of fluid dynamics have indicated that the generation of turbulence in an axisymmetric jet flow is related to small-amplitude body forces causing perturbations in the unstable shear layers at the jet exit, which grow as they move downstream.[13–17]

To characterize the chemical species produced downstream of the jet orifice, multiple invasive and noninvasive diagnostic techniques have been applied, including tunable diode laser absorption spectroscopy,[18] mass spectroscopy,[19] Fourier transform infrared spectroscopy,[20] laser-induced fluorescence (LIF), and two-photon absorption laser-induced fluorescence.[21–23] Of all the techniques investigated, LIF based methods are particularly convenient as they provide the high spatio-temporal resolution required to accurately investigate the complex downstream chemistry in a plasma jet while facilitating the quantification of absolute radical densities. Regardless of the diagnostic technique used, it is clear that a significant proportion of the reactive chemical species produced within the downstream region of the jet is a result of reactions between the noble gas plasma and molecular gas impurities entrained from the surrounding environment, which is typically humid air. Given that the interplay between the propagating plasma plume and the ambient environment has a considerable impact on the physicochemical properties of the plasma jet and, therefore, on the application efficacy, understanding the underpinning mechanisms of how air becomes entrained within the flowing noble gas channel is of vital importance.

This study investigates the entrainment of air into a helium plasma jet and explores the hypothesis that small perturbations within the jet shear layer resulting from plasma generation not only result in the early onset of turbulence but also act to increase entrainment of air into the laminar region of the jet. Particle image velocimetry (PIV) was used to quantify the fluid dynamics of the helium jet flow beyond the jet orifice and combined with LIF to provide a sensitive means of assessing the entrainment of humid air into the discharge.

2 | EXPERIMENTAL AND COMPUTATIONAL METHODS

2.1 | Plasma jet and PIV setup

The plasma jet used in this study comprised of a quartz capillary with an inner diameter D, equal to 3 mm and an outer diameter of 5 mm, a metallic strip was wrapped around the outer diameter of the capillary to act as a ground electrode, as shown in Figure 1. A tungsten pin was positioned coaxially within the quartz capillary and

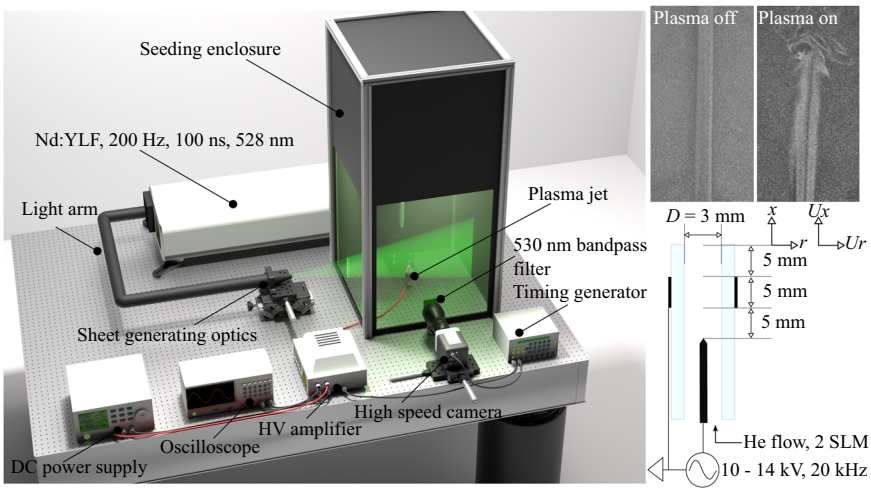

FIGURE 1 Diagram showing the layout of the particle image velocimetry experiment and configuration of the plasma jet device, with representative particle image velocimetry images for the plasma off and plasma on cases, vectors U_x and U_r represent the axial and radial velocity components, respectively

connected to a high-voltage sinusoidal power source operating at a frequency of 20 kHz. Two applied voltage cases were examined in this study, 14 and 10 kVpp, with the latter being just above the point of gas breakdown. Helium gas with a purity of 99.999% was flushed through the capillary at 2 standard liters per minute (SLM), giving a maximum exit velocity, U_m, equal to 9.4 m/s.

To quantify the flow field created by the plasma jet, PIV measurements were undertaken using the experimental setup shown in Figure 1. The plasma jet was inserted into a large sealed chamber (volume >2 m^3), which was seeded using oil droplets with a nominal size of 1 μm. The chamber ensured that the plasma jet flow was not influenced by any external draughts. A similar experimental arrangement was used in the previous studies of the authors,[8] where it was observed that an insufficient number of seeding particles were entrained within the laminar region of the jet to obtain reliable PIV measurements. To overcome this challenge, the helium flow into the jet capillary was seeded using oil droplets, which also had a nominal size of 1 μm. The addition of oil droplets to the helium gas flow has an obvious potential to disrupt the discharge; while such changes are difficult to assess, the breakdown voltage and length of plasma plume were found not to change significantly. Furthermore, Rayleigh scattering was used to obtain an approximate indication of the laminar region length in an unseeded jet and a close agreement was observed when compared with the PIV measurements on the seeded jet, suggesting the presence of the seeding particles had a minimal impact on the fluid dynamic properties of the system. Given the nominal size of the seeding particles, the Stokes number was found to be less than 0.1, thus ensuring that the particles followed the fluid flow closely with tracing errors being <1%.[24]

Planar velocity measurements were conducted using a two-dimensional (2D) particle image velocimetry system from TSI Inc. The system consisted of a double-pulsed Nd:YLF laser operating at 200 Hz with a pulse duration of 100 ns at a wavelength of 527 nm and was used to generate a 1-mm thick light sheet that was projected into the seeding chamber and across the plasma jet orifice. A high-speed Phantom Miro Lab 340 camera was positioned outside the seeding chamber normal to the laser sheet and synchronized with the laser such that each frame captured a single laser pulse. A spatial calibration was performed and the time delay between consecutive laser pulses (Δt) was set to 30 μs, a value chosen to capture the movement of oil droplets over a grid with spatial dimensions of 350 μm^2, enabling the velocity vectors to be computed using a recursive cross-correlation technique. For each measurement condition, the plasma jet was operated for several seconds before data capture to ensure steady-state conditions were achieved. Each data set comprised of 800 frames that were used to make 400 individual velocity vector maps; in the case of time-averaged measurements, all 400 vector maps were averaged and presented as a single figure.

2.2 | LIF setup and OH density calibration

The LIF measurement system used in the investigation is shown in Figure 2, the system was used to measure OH

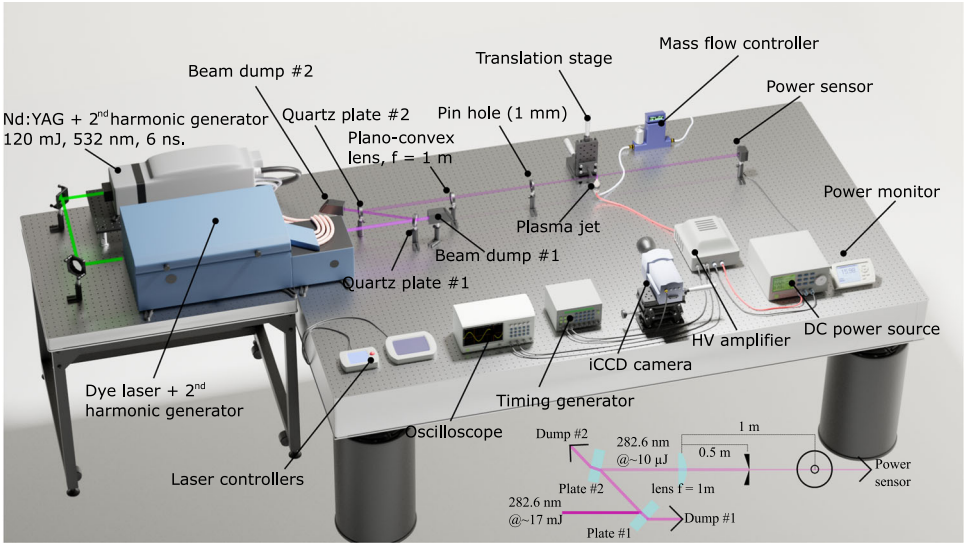

FIGURE 2 Diagram showing the layout of the laser-induced fluorescence experiment, insert highlights optical arrangement used to achieve a three-order reduction in laser intensity

radical density and to obtain an indication of air entrainment within the plasma plume through the measurement of the radiative decay time of the laser-excited OH(A) state. The system comprised of a tunable dye laser (Sirah Cobra Stretch with second harmonic generation unit) pumped by a 6-ns pulsed Nd:YAG laser with a wavelength of 532 nm, pulse energy of 120 mJ, and a repetition rate of 10 Hz. A number of LIF excitation schemes have been proposed for the measurement of OH radicals in atmospheric pressure plasmas.[25–27] In this study, the dye laser was tuned to generate an output at a wavelength 282.58 nm to excite the $P_1(2)$ transition from the $f_1(2)$ rotational level of OH $X(v'' = 0)$ to the $f_1(1)$ rotational level of OH $A(v' = 1)$. Several previous studies have used a similar excitation scheme due to the $P_1(2)$ transition being spectrally separated from adjacent lines, and the $f_1(2)$ level having the largest relative population in the temperature range under investigation.[28]

The 282.58-nm beam emitted from the dye laser was measured to have a pulse energy in excess of 17 mJ, a value several orders of magnitude above the range linear LIF measurements are typically made (1–10 μJ).[29] Operation beyond the linear region greatly complicates the interpretation of the results, as the ground rotational level is significantly depleted by light absorption and partially refilled by fast rotational redistribution, altering the LIF outcome dependent on the unknown gas composition and temperature. To attenuate the laser energy to a suitable range an optical arrangement similar to that employed by Riès et al.[21] was adopted, two quartz plates were angled to split the beam as shown in Figure 2, with a small fraction being reflected towards the plasma jet and the majority of the beam passing through to beam dumps mounted behind each plate. Following attenuation, the beam was directed through an uncoated quartz plano-convex lens with a focal length of 1 m, and a pinhole of 1 mm was positioned to act as a spatial filter, further attenuating the beam. Using this approach, the maximum laser pulse energy was found to be approximately 15 μJ; small changes to the Q-switch delay of the pump laser were subsequently used to vary the pulse energy between 1 and 15 μJ. Laser power was measured using a Thorlabs PM100D optical power and energy meter equipped with a thermal volume absorber power sensor.

To capture the fluorescence of excited OH molecules, an Andor iStar740 ICCD camera was fitted with a Jenoptik UV 105 mm f/4.5 imaging lens. The camera arrangement was positioned to face the plasma jet perpendicular to the laser beam. For each image recorded, the ICCD camera was configured to accumulatively capture 500 laser pulses, using an optical gate width equal to 8 ns for each exposure. Following the approach of Verreycken et al.,[28] no bandpass filter was used during LIF measurements to avoid the need for additional corrections in the calibration procedure. A consequence of this approach is the potential for interference of the fluorescent signal from other emissions within the plasma and the Rayleigh scattering signal. Background subtraction of the emission captured with the plasma energized and laser detuned was used to correct for light emitted by the plasma and any scattered light. To ensure the measurements were conducted within the linear LIF region, the measured LIF intensity was plotted against laser energy and a linear fit applied. It was determined that the linear range was between 1 and 10 μJ, a value in close agreement with several past LIF investigations.[21,28]

Absolute calibration of the LIF signal to determine the density of ground-state OH can be achieved via several methods, including UV absorption, chemical modeling, and Rayleigh scattering.[28,30] In this investigation, the Rayleigh scattering approach was adopted due to its high degree of accuracy, and a similar methodology to that described by Verreycken et al.[28] was adopted. Calibration by Rayleigh scattering requires detailed knowledge of the rotational and vibrational energy transfer rates, which vary significantly depending on the nature of the quenchers present; thus, an accurate appreciation of the gas composition is essential. Careful consideration must be applied in the case of a plasma jet as the gas composition varies as a function of distance from the jet orifice; further details on this are provided in Section 2.3. Also important for the determination of absolute OH density is the decay time of the laser-excited fluorescent state. This was measured at each spatial position by applying a time delay to the ICCD camera from 6 ns (i.e., immediately after the laser pulse) up to 2,000 ns; at each time point, the fluorescent intensity from 500 laser shots was accumulated to form a single image. From each image, the sum of the LIF intensity in a 0.36 mm^2 interrogation area on the jet centreline was determined and plotted as a function of delay time, an exponential fit was applied to determine the decay rate at each spatial position.

In addition to the gas composition, the gas temperature can also affect the interpretation of the LIF data. To investigate the influence of plasma generation on gas temperature, an Omega FOB100 fiber-optic thermometer was used, the dielectric temperature probe was positioned in the plasma at various points downstream of the jet orifice and the temperature recorded. The temperature was found to vary little with spatial position, with a maximum of 10 K above ambient located close to the capillary orifice, such observations are in line with previous studies.[8]

TABLE 1 Experimental parameters used in laser-induced fluorescence measurements and absolute density calibration

Parameter	Description	Value
λ_L	Laser wavelength	282.58 nm
$\Delta\lambda_L$	Linewidth of the laser	0.95 pm
g_{int}	Overlap integral	0.017 m
A_L	Area of the laser beam	0.0746 mm^2
E_L	Laser energy per pulse	10 μJ
τ_L	Temporal FWHM of the laser pulse	6 ns
Δx	Length of the detection volume	0.359 mm
Δy	Width of the detection volume	0.359 mm
Δs	The spatial FWHM of the laser beam at the observation point	0.1795 mm

Abbreviation: FWHM, full width at half maximum.

The remainder of the calibration process closely followed that reported previously by Verreycken et al.[28] and will only be summarized in brief here. To obtain Rayleigh scattering data for calibration, the jet capillary was supplied with Nitrogen gas at a flow rate of 2 SLM, while not strictly necessary, the nitrogen flow helped to ensure dust from the ambient environment did not enter the measurement region of interest. The laser power was varied from 2 to 15 μJ in 1-μJ increments, and the sum of the Rayleigh scattered signal intensity in a square region of interest measuring 0.36 mm^2 was calculated. The measured Rayleigh scattered signal, S_{Ray} (#counts), can be written as:

$$S_{Ray} = \eta N_n \frac{\partial^{\beta=0}\sigma_0}{\partial\Omega} V_{Ray} I_L t_L, \quad (1)$$

where η is the calibration constant (#counts sr/J), N_n is the density of scattering particles (m^{-3}), $\partial^{\beta=0}\sigma_0/\partial\Omega$ is the differential cross-section for Rayleigh scattering (m^2/sr), V_{Ray} is the volume from which Rayleigh scattering is collected (m^3), I_L is the laser irradiance (W/m^2) and t_L is the temporal length of the laser pulse (s), which was measured by replacing the power meter shown in Figure 2 with a fast photodetector. After considering the non-uniformity of the laser energy density, Equation (1) becomes:

$$S_{Ray} = \eta N_n \frac{\partial^{\beta=0}\sigma_0}{\partial\Omega} E_L \Delta x, \quad (2)$$

where E_L is the laser energy (J), and Δx is the length of the detection volume (m). Following this, the calibration constant η was obtained from the slope α, of the measured Rayleigh intensity as a function of laser energy multiplied by pressure:

$$\eta = \alpha k_B T \frac{\partial^{\beta=0}\sigma_0}{\partial\Omega} \Delta x, \quad (3)$$

where k_B is the Boltzmann constant and T is the temperature (K). Using the calibration factor, the intensity of the laser-induced fluorescence S_{LIF}, can be expressed as:

$$S_{LIF} = \frac{1}{4\pi} \int \eta E n_{exc}(x, y, z, t) A dx dy dz dt, \quad (4)$$

where E is the energy gap according to the chosen transition, A is the Einstein emission coefficient (s^{-1}), and n_{exc} (x, y, z, t) is the density of OH in the excited state. To determine the ground-state OH density based on n_{exc} in Equation (4), the four-level collisional radiative model reported by Verreycken et al.[28] was utilized. Briefly, the model follows the densities of 3 laser-excited levels of OH in addition to the ground-state. The followed levels are the ground-state OH $X(v''=0)$, OH $A(v'=1)$, OH $A(v'=0)$, and OH $X(v''=1)$. For each level an ordinary differential equation is solved describing the gains and the losses of that level, leading to a coupled system of four equations. The processes described in the system are the radiative excitation by the laser, the quenching by air constituents, and the vibrational relaxation. It is assumed in the model that the rotational energy transfer is much faster than the other processes; thus, the rotational levels are not resolved. The inputs to the four-level model include the experimental parameters listed in Table 1, the gas composition determined by the flow model described in Section 2.3, and an estimated ground-state OH density. Solving the four-level model provides a prediction of the LIF signal intensity, which by comparison with the measured LIF signal intensity is used to determine the actual ground-state OH density. Full details of the implementation can be found in the studies of Verreycken et al.[28] Finally, Table 1 shows the relevant experimental parameters used in the LIF measurements, and these were also used as inputs for the computational model.

2.3 | Computational model and statistical analysis methodology

To account for the varying composition of gas downstream of the jet orifice, a computational model was developed that solved for the velocity field of the gas mixture in addition to the mass fractions of its

constituents, namely N_2, O_2, H_2O, and He. To obtain the velocity field, the model solved the mass continuity Equation (5), which solves for the mass density of the entire gas mixture, and the momentum conservation Equation (6). To compute the densities of the species constituting the gas mixture, the continuity equation, given by Equation (7), was solved for the mass fraction of three species, while the mass fraction of the fourth was determined from the pressure constraint. All equations were solved in steady-state mode (i.e., time-independent equations):

$$\nabla \cdot (\rho \vec{u}) = 0, \tag{5}$$

$$\rho(\vec{u} \cdot \nabla)\vec{u} = -\nabla p + \nabla \cdot \left(\mu(\nabla \vec{u} + \nabla \vec{u}^T) - \frac{2}{3}\mu(\nabla \cdot \vec{u})I\right) - (\rho - \rho_0)g, \tag{6}$$

$$\rho(\vec{u} \cdot \nabla)\omega_i + \nabla \cdot (\vec{\Gamma_i}) = 0, \tag{7}$$

where ρ is the density of the gas mixture (kg/m^3), $\vec{u}$ is the velocity field of the gas mixture (m/s), p is the gas mixture's pressure (Pa), μ is the gas mixture's viscosity (Pa s), I is the identity matrix, ρ_0 is the density of air (kg/m^3), and g is the gravitational constant (m/s^2), ω_i is the mass fraction of the ith species, and Γ_i is the diffusive flux of the ith species, which is calculated according to the Maxwell–Stefan theory for diffusion as given by Equation (8)–(10).[31,32]

$$\vec{\Gamma_i} = \rho \omega_i \vec{V_i}, \tag{8}$$

$$\nabla x_i = \sum_{j=1}^{4} \frac{x_i x_j}{D_{ij}}(\vec{V_j} - \vec{V_i}) + \frac{\nabla p}{p}(\omega_i - x_i), \tag{9}$$

$$x_i = \frac{M_n}{M_i}\omega_i, \tag{10}$$

where $\vec{V_i}$ is the diffusion velocity of the ith species (m/s), x_i is the mole fraction of the ith species (dimensionless), which is related to the mass fraction by Equation (10) and D_{ij} is the binary diffusion coefficients between the ith and the jth species (m^2/s). A list of the binary diffusion coefficients used in the model is given in Table 2. It should be noted that Equation (9) is incorporated in the model as a constraint linking the flux term and the mass fraction term in Equation (7). In Equation (10), M_i and M_n are the molecular weight of the ith species and the average molecular weight, respectively (kg/mol). Finally, the computational domain and the boundary conditions used are described in the Supporting Information.

As stated in the introduction section, it is hypothesized that plasma-induced turbulence affects the flow's velocity field and thus the gas composition. To account for such effects in the computational model, the Reynolds-Averaged Navier-Stokes (RANS) approach for modeling turbulence was followed, where a turbulent viscosity μ_T (also known as eddy viscosity) was added to the viscosity of the gas mixture. The eddy viscosity is a mathematical means to describe the loss of momentum of the flow as a result of turbulence as an "effective" viscosity that is added to the physical viscosity of the fluid. Similarly, a turbulent diffusivity D_T is added to the binary diffusion coefficients.[32] The computation of the eddy viscosity is typically done using one of the conventional RANS turbulence models, such as the k–ε model. Considering that such models were calibrated for flows without plasma, their use for plasma-modified flows will yield results with unknown accuracy. To overcome this challenge, statistical analysis of the PIV data was conducted to obtain the necessary parameters to calculate the eddy viscosity resulting from the plasma generation. Following the k–ε modeling approach, the turbulent kinetic energy k (m^2/s^2) and the turbulent kinetic energy dissipation rate ε (m^2/s^3) are defined by Equations (11) and (12).[36]

$$k = \frac{1}{2}\left(\overline{u'^2_r} + \overline{u'^2_x}\right), \tag{11}$$

$$\varepsilon = 2\upsilon \overline{s'_{ij} \cdot s'_{ij}}, \tag{12}$$

where u'_r and u'_x are the time-fluctuating velocity field components with respect to the average velocity field, which were calculated from PIV data by subtracting the time-averaged velocity field from each of the 400 instantaneous velocity maps captured during a measurement, then averaging the square of these fluctuations. In Equation (12), υ is the kinematic viscosity (m^2/s), and s'_{ij} is the fluctuating deformation rate of the fluid (s^{-1}), which was calculated from the PIV data as outlined by Xu et al.[37] After calculating k

TABLE 2 A list of binary diffusion coefficients used in the model

Combination	Diffusion coefficient (m^2/s)	Reference
N_2–He	6.78×10^{-5}	[33]
N_2–O_2	2.09×10^{-5}	[34]
N_2–H_2O	2.54×10^{-5}	[35]
O_2–He	7.36×10^{-5}	[33]
He–H_2O	8.36×10^{-5}	[35]
O_2–H_2O	3.185×10^{-5}	[35]

and ε the eddy viscosity was calculated according to Equation (13).[36]

$$\mu_T = \rho C \frac{k^2}{\varepsilon}, \tag{13}$$

where C is a constant equal to 0.0016 and ρ is the self-consistent gas mixture density calculated by the model. The turbulent diffusivity D_T is related to the eddy viscosity by Equation (14).[28]

$$D_T = \frac{\mu_T}{\rho Sc_T}, \tag{14}$$

where Sc_T is the turbulent Schmidt number, obtaining an accurate value for this in a plasma-modified flow is not possible; however, the turbulent Schmidt number is close to unity for a wide variety of gas flows under very diverse conditions; hence it is assumed to be 1 in this investigation.[38] The model was subsequently solved with the experimental input of μ_T and D_T, which were smoothed and mirrored, then added to their physical counterpart quantities. The model was solved for both applied voltage cases investigated in this study, in addition to an unperturbed laminar case, where the eddy viscosity and diffusivity were set to 0.

As described in Section 2.2, the radiative collisional model consisted of a system of ordinary differential equations (ODE) describing the LIF transitions. The system was solved at every point in the computational domain close to the jet's orifice ($x < 20$ mm, $x/D < 7$), with the gas composition required for the ODEs being taken from that calculated by the fluid flow model. To quantify the density of ground-state OH, the four-level model reported by Verreycken et al.[28] was adopted. To validate the developed computational model, the predicted LIF signal decay times were compared with those measured experimentally at multiple points along the jet axis; a close agreement was observed and is further discussed in the results section.

3 | RESULTS AND DISCUSSION

3.1 | Influence of plasma on jet velocity and turbulence generation

PIV measurements were undertaken to quantify the velocity of the flowing helium gas and the resulting perturbation of the surrounding quiescent air beyond the jet orifice. Figure 3a–c shows the ensemble-averaged two-component velocity vector maps and velocity magnitude (U) normalized to the measured exit velocity (U_m) for the 0, 10, and 14-kV cases, respectively. Without a plasma discharge (0-kV case), the undisturbed helium flow appeared laminar over the entire measurement region, confirmed by the ensemble-averaged centerline velocity (U_c) profile in Figure 3d. On the application of a 10-kV sinusoidal waveform, a weak discharge was observed to form, indicating gas breakdown had been achieved;

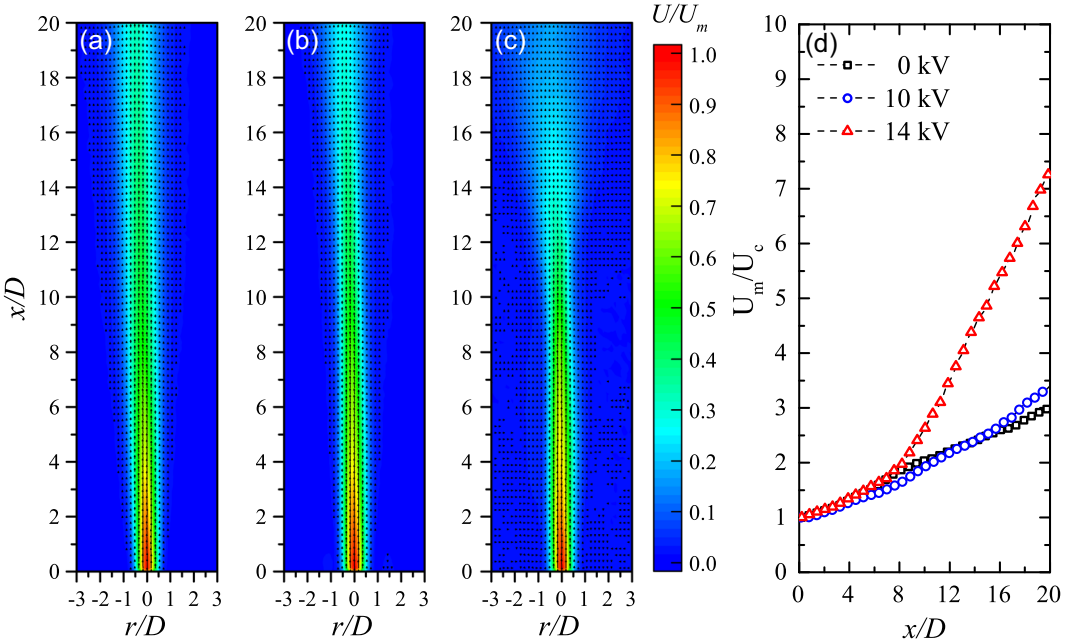

FIGURE 3 Ensemble-averaged particle image velocimetry measurements of the plasma jet obtained at applied voltages of (a) 0 kV, (b) 10 kV, and (c) 14 kV, (d) shows the reciprocal of the ensemble-averaged centerline velocity (U_c) normalized to the measured exit velocity (U_m)

under such conditions, little obvious change to the velocity profile was observed. An increase in applied voltage from 10 to 14 kV led to an increase in the length of the visible plasma plume. Comparing Figure 3b and 3c, highlights the impact of the applied voltage on the flow structure downstream of the jet orifice, with the higher applied voltage resulting in a significant reduction in the length of the laminar flow region. From the ensemble-averaged centerline velocity, an abrupt change in gradient is observed at approximately 8 *x/D*, indicating a transition to turbulence. Though such results are perhaps the first-quantitative measurements of velocity within a plasma jet, they are highly consistent with previous observations made using qualitative methods such as Schlieren imaging.[9,39]

In absolute terms, the generation of plasma with an applied voltage of 14 kV was found to increase U_m by 0.94 m/s, representing a relatively modest increase of approximately 10% compared to the 0-kV case. Such increases in velocity are in line with those predicted by others and are a consequence of gas heating and electrohydrodynamic forces induced by the plasma, with the latter mechanism being the most likely dominant factor.[8,11] Notably, the modest change in velocity associated with plasma generation cannot directly explain the transition to turbulence observed when comparing Figures 3a and 3c. Past studies on turbulence generation in axisymmetric round jets have revealed that turbulence initiates due to instabilities within the shear layers at the jet exit that become amplified as they travel downstream.[13–17] As the instabilities grow, they cause velocity fluctuations, Reynolds shear stresses, and thus the production of turbulence.[8] Many previous studies have explored "excited" jets that employ alternative means to perturb the jet flow to investigate the mechanisms of turbulence generation.[40–45] For example, the impact of sonic excitation on the jet velocity profile shows a remarkable similarity to those observed in this study[41]; hence, it is posited that plasma generation is an alternative means to excite an axisymmetric round jet, resulting in the rapid onset of turbulence through increased shear-layer instability with little change to velocity.

Though the growth of small-scale instabilities within the jet shear layer has a significant impact on the laminar to turbulent transition, they also provide a mechanism to enhance entrainment of quiescent air into the laminar region of the plasma jet.[45] To investigate the influence of plasma generation on instabilities in the jet shear layer, the eddy viscosity μ_T was calculated. The eddy viscosity profiles for the two plasma cases investigated in this

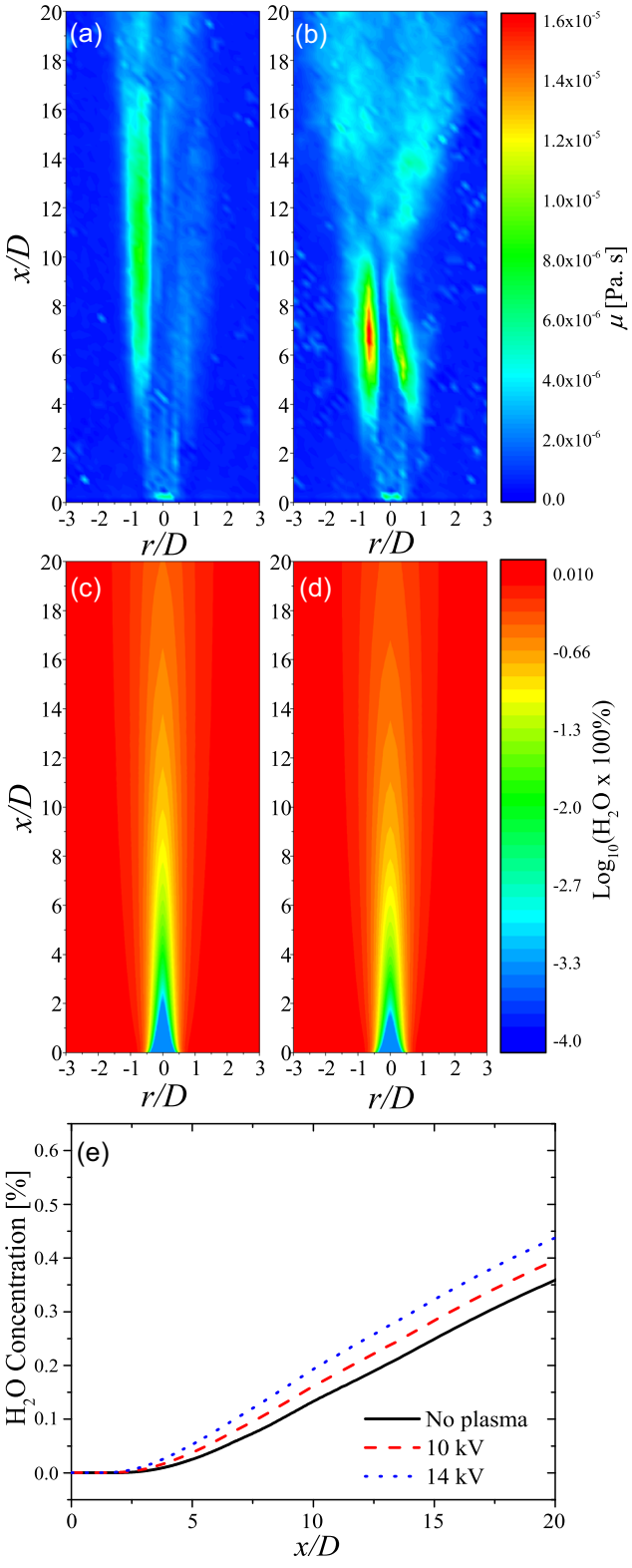

FIGURE 4 Eddy viscosity calculated from PIV measurements for the (a) 10-kV and (b) 14-kV excited plasma jet and the calculated percentage of H_2O in the helium flow under (c) 0-kV and (d) 14-kV conditions. (e) Percentage of H_2O along the jet centerline for all three cases

study are shown in Figure 4a,b. Three characteristic zones can be observed within the profiles, the first is close to the jet orifice, where a region of low μ_T exists, which can be explained by the fact that this is the laminar region where the amplitude of velocity fluctuations is small, leading to low turbulent kinetic energy k, and consequently, a low μ_T as Equation (13) shows. The second zone (e.g., 4–10 x/D in Figure 4b) coincides with the transition region, as inferred from Figure 3d, where the value of μ_T peaks. This is attributed to the large scale fluctuations/eddies starting to appear in the transition region, leading to high turbulent kinetic energy k, and considering that such large fluctuations live long enough to be transported downstream, the dissipation rate of the turbulent energy ε is relatively low in this region, thus leading to a peak of μ_T, as follows from Equation (13). The third zone (e.g., >10 x/D in Figure 4b) coincides with the turbulent region, as inferred from Figure 3d, which has a moderate value of μ_T. As known from the energy cascade theory of turbulence,[46] the large eddies generated in the transition region break into smaller eddies in the fully turbulent region, the small eddies are dissipated into heat due to the physical viscosity of the fluid.[46] In this sense, the turbulent kinetic energy k is high, whereas the turbulent dissipation rate ε is also high, leading to a moderate value of μ_T.

From Figure 4a,b, it is clear that the eddy viscosity for the 14-kV case has a larger magnitude compared to the 10-kV case, which is consistent with the PIV results presented in Figure 3b,c. When comparing the average value of μ_T in zone one ($x/D < 4$) for both cases, it is found that μ_T for the 10-kV case is approximately 70–80% of that for the 14-kV case, indicating that the plasma's perturbation to the flow in the laminar region is more significant for the 14-kV case in comparison to the 10-kV case.

As described in Section 2.3, a higher value of the eddy viscosity of μ_T indicates a higher value of eddy diffusivity D_T, which adds to the physical diffusion coefficients, leading to increased entrainment of air into the helium jet for higher values of μ_T. To highlight the impact of the plasma-induced entrainment, Figures 4c and 4d show the computed percentage of H_2O in the gas mixture for the 0- and 14-kV cases, respectively. Notably, the 0-kV case represents an unperturbed laminar flow where quiescent air is entrained due to the physical diffusion only. However, in the case of the perturbed flow shown in Figure 4d, air entrainment occurs due to physical diffusion plus the "effective" eddy diffusion due to turbulence. The centerline concentration of H_2O, shown in Figure 4e, was set to 0.00004% for all cases, a value obtained from the helium gas provider. Moving downstream to 2 x/D, the level of H_2O in the unperturbed 0-kV case was found to increase to be approximately 0.0005%. In contrast, the H_2O concentration in the perturbed case was found to be 0.0034%, representing a seven-fold increase. Further downstream at 6 x/D, the H_2O concentration in the unperturbed case was found to be 0.046%, compared to 0.082% in the perturbed case, representing a 1.8-fold increase. When moving downstream, the difference between the unperturbed case and the 14-kV perturbed case diminishes as a result of the increasing density of the gas mixture, which lowers the value of the eddy diffusivity as defined by Equation (4).

3.2 | OH fluorescence decay rate and absolute density

As described by Yonemori et al.[47] the decay rate of the LIF signal from OH provides a sensitive indication of the helium-air mixing ratio as the quenching rate of the laser-excited state is strongly influenced by the density of quenching species present within the flowing helium gas (e.g., N_2, O_2, and H_2O). In this study, a comparison between the measured LIF decay rate and computed decay rate by the model was used to validate the adopted computational approach describing plasma-induced entrainment, thus enabling the accurate quantification of absolute OH density downstream of the jet exit. The decay time is obtained from the fitting of the temporal evolution of the LIF signal intensity, as described in Section 2.3. Figure 5 shows the measured and computed LIF decay time as a function of downstream spatial position for both the 10- and 14-kV cases; additionally, the predicted decay time for a hypothetical unperturbed (laminar) helium flow is shown. The LIF decay time is

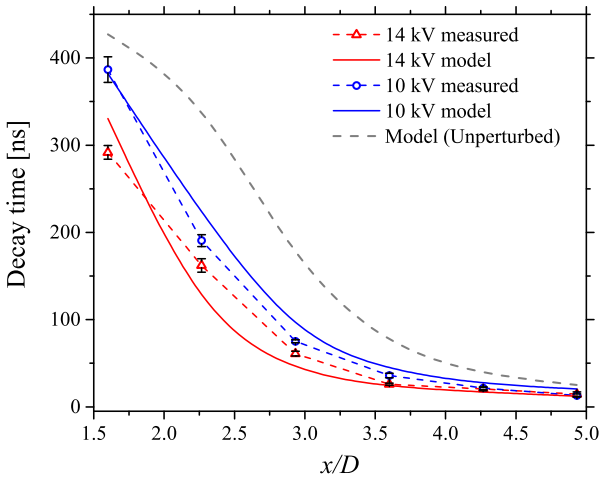

FIGURE 5 Comparison between measured and calculated decay time of the laser-induced fluorescent signal as a function of downstream distance from the jet orifice

shorter at all spatial positions under both 10- and 14-kV excitation compared to what would be observed under idealized laminar conditions. As highlighted in Figure 4c,d, plasma generation increases air entrainment, which acts to increase the density of quenchers and thus increase the quenching rate of the OH-fluorescent state. This result provides experimental evidence supporting the hypothesis that plasma generation increases the entrainment of air within the helium jet at all spatial positions, not just the fully turbulent region. The calculated decay times closely match the measured data points, with both cases showing the agreement.

Using the experimental procedure outlined in Section 2.2, the 2D LIF emission profile was compiled for both the 10- and 14-kV cases and is shown in Figures 6a and 6b, respectively. By comparing the centerline LIF intensity obtained from the 2D profile and the computed LIF intensity from the collisional radiative model, the absolute ground-state OH density was calculated as a function of downstream position from the jet exit, shown in Figure 6c. Consistent with the observations made in many previous studies, an increase in applied voltage was observed to increase the peak OH density within the plasma plume.[26] Given that hydrogen-based species densities increase when the air/water vapor fraction increases,[48] it becomes likely that an increase in the applied voltage results in an increase in OH density as a result of not only more intense discharge conditions but also increased entrainment of air and H_2O. Critically, the position of peak OH density was found to vary depending on the applied voltage. This phenomenon is attributed to the interplay between the physical properties of the plasma (i.e., n_e and T_e) and the fluid dynamics of the helium jet. With an applied voltage of 14 kV, perturbations within the jet shear layer caused by plasma generation induce an early transition to a turbulent flow regime, as confirmed in Figures 3 and 4. Under such conditions, the generation of OH close to the jet exit is locally enhanced due to enhanced H_2O entrainment combined with the relatively intense discharge conditions. Beyond the local maxima, the elevated air mole fraction as a result of the enhanced entrainment acts to quench the discharge and thus impedes OH generation. Conversely, at the lower applied voltage of 10-kV, the discharge is comparatively less intense, meaning, less air entrainment and a weaker plasma is formed, both factors contributing to limit OH production. However, less shear-layer perturbation causes less air entrainment into the helium flow; thus, the discharge can propagate further from the orifice. Consequently, the concentration of ground-state OH is significantly higher far downstream from the jet exit in the 10-kV case compared to the 14-kV case.

The presented findings have considerable implications from a practical perspective as it has been demonstrated that the density of OH at a given downstream position is strongly influenced by both the discharge characteristics and its interaction with the quiescent background gas. Though it is generally assumed that a higher plasma generation voltage results in enhanced production of OH, Figure 6 clearly shows that this only holds true close to the jet orifice. With increasing voltage comes increasing entrainment, which ultimately begins to quench the discharge and negatively affects downstream OH production. Counterintuitively, Figure 6c indicates that at a position of 5.3 x/D (i.e., 16 mm from the jet exit), there is an order of magnitude more OH from a plasma generated using 10-kV compared to one generated using 14-kV excitation. These findings demonstrate that the complex interplay between the physicochemical properties of the

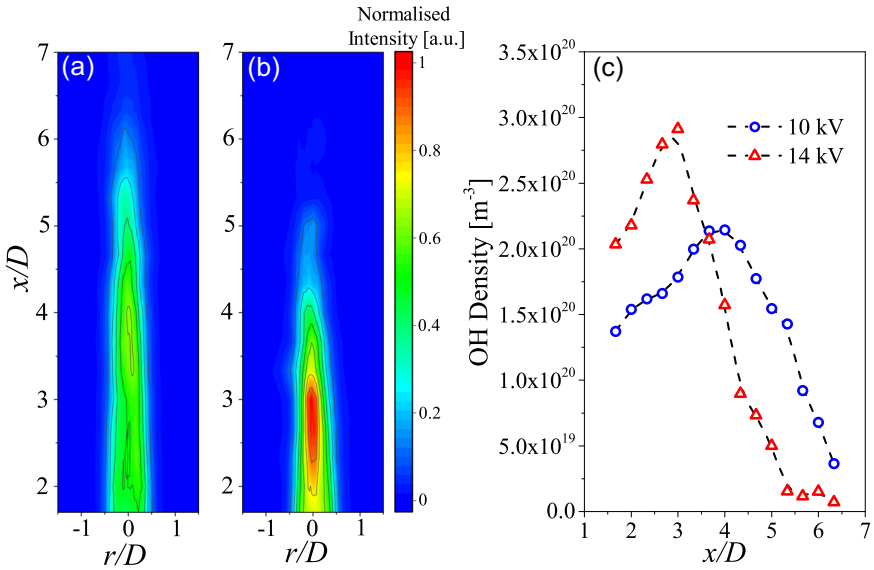

FIGURE 6 Composite two-dimensional normalized laser-induced fluorescence intensity for (a) 10-kV and (b) 14-kV cases. Absolute centerline OH density for the 10- and 14-kV case as a function of distance from the jet orifice

plasma and the fluid dynamic properties of the flowing noble gas must be carefully considered when designing plasma jet sources for use in applications such as biomedicine and materials processing.

4 | CONCLUSION

This contribution has employed PIV, LIF, and computational fluid dynamics to explore the interplay between the propagating plasma plume and the quiescent background air in an axisymmetric dielectric barrier discharge jet. Despite the rapid onset of turbulence observed following plasma ignition, it was demonstrated that the presence of the plasma had little impact on the jet exit velocity of the helium flow. Through statistical analysis of the measured velocity field from the plasma jet under varying excitation conditions, it was determined that plasma generation resulted in shear-layer perturbations that grow downstream to initiate the early onset of turbulence.

Using the experimentally derived eddy viscosity, a computational model was developed to calculate the density of humid air entrained within the helium jet flow. To validate the model, the calculated decay time of the laser-induced fluorescent state of OH was compared against those measured experimentally and found to be in good agreement. Finally, the computational model was used to convert the measured LIF intensity into an absolute OH density from which it was concluded that OH production is strongly influenced by the interplay between the propagating plasma and the background air. At high applied voltages, it was found that OH density increases close to the exit but is rapidly reduced downstream as a result of the elevated air content quenching the discharge.

In summary, this study demonstrates an intricate link between the physicochemical properties of the plasma and its interaction with the quiescent air. As many applications rely on the presence of RONs, which are predominantly formed when the plasma interacts with the background environment, the results of this study provide valuable insight into the underpinning mechanisms governing these interactions.

ACKNOWLEDGMENTS

JLW and MIH would like to acknowledge the support of the Engineering and Physical Sciences Research Council (Projects EP/S025790/1, EP/S017623/1, EP/R041849/1, and EP/N021347/1). RDW would like to acknowledge the support of the NATO AVT-254 plasma flow control group.

ORCID

Youssef Morabit http://orcid.org/0000-0003-2337-6257
Richard D. Whalley http://orcid.org/0000-0001-6388-5895
Eric Robert http://orcid.org/0000-0002-7894-7080
Mohammad I. Hasan http://orcid.org/0000-0001-6993-933X
James L. Walsh http://orcid.org/0000-0002-6318-0892

REFERENCES

[1] A. J. Knoll, P. Luan, A. Pranda, R. L. Bruce, G. S. Oehrlein, *Plasma Process. Polym.* **2018**, *15*, 1700217. https://doi.org/10.1002/ppap.201700217
[2] X. Deng, A. Yu Nikiforov, T. Coenye, P. Cools, G. Aziz, R. Morent, N. De Geyter, C. Leys, *Sci. Rep.* **2015**, *5*, 10138. https://doi.org/10.1038/srep10138
[3] P. B. Flynn, S. Higginbotham, N. H. Alshraiedeh, S. P. Gorman, W. G. Graham, B. F. Gilmore, *Int. J. Antimicrob. Agents* **2015**, *46*, 1. https://doi.org/.org/10.1016/j.ijantimicag.2015.02.026
[4] H. Tanaka, M. Mizuno, K. Ishikawa, S. Toyokuni, H. Kajiyama, F. Kikkawa, M. Hori, *Plasma* **2018**, *1*, 1. https://doi.org/10.3390/plasma1010014
[5] S. Bekeschus, P. Favia, E. Robert, T. Von Woedtke, *Plasma. Process. Polym.* **2019**, *16*, 1800033. https://doi.org/10.1002/ppap.201800033
[6] S. Iseni, A. Schmidt-Bleker, J. Winter, K.-D. Weltmann, S. Reuter, *J. Phys. D: Appl. Phys.* **2014**, *47*, 152001. https://doi.org/10.1088/0022-3727/47/15/152001
[7] T. Darny, J. M. Pouvesle, J. Fontane, L. Joly, S. Dozias, E. Robert, *Plasma Sources Sci. Technol.* **2017**, *26*, 105001. https://doi.org/10.1088/1361-6595/aa8877
[8] R. D. Whalley, J. L. Walsh, *Sci. Rep.* **2016**, *6*, 31756. https://doi.org/10.1038/srep31756
[9] R. Xiong, Q. Xiong, A. Y. Nikiforov, P. Vanraes, C. Leys, *J. Appl. Phys.* **2012**, *112*, 033305. https://doi.org/10.1063/1.4746700
[10] M. Boselli, V. Colombo, E. Ghedini, M. Gherardi, R. Laurita, *Plasma Chem. Plasma Process.* **2014**, *34*, 853. https://doi.org/10.1007/s11090-014-9537-1
[11] S. Park, U. Cvelbar, W. Choe, S. Y. Moon, *Nat. Commun.* **2018**, *9*, 371. https://doi.org/10.1038/s41467-017-02766-9
[12] M. I. Hasan, J. W. Bradley, *J. Phys. D: Appl. Phys.* **2016**, *49*, 055203. https://doi.org/10.1088/0022-3727/49/5/055203
[13] A. Michalke, *Journal of Fluid Mechanics* **1964**, *19*, 543–556. https://doi.org/10.1017/s0022112064000908
[14] A. Michalke, *J. Fluid Mech.* **1965**, *23*, 3. https://doi.org/10.1017/S0022112065001520
[15] M. Lessen, *Nat. Adv. Comm. Aero., Wash.* **1950**, Tech. Rep. no. 979.

[16] A. Michalke, R. Wille, *Applied Mechanics, Proceedings of the 11th International Congress Applied Mechanics Munich*, (Eds: H. Görtler), Springer-Verlag, Berlin-Heidelberg-New York 1966, pp. 962–972.
[17] A. Michalke, *Prog. Aerosp. Sci.* **1972**, *12*, 213. https://doi.org/10.1016/0376-0421(72)90005-X
[18] A. V. Pipa, T. Bindemann, R. Foest, E. Kindel, J. Röpcke, K.-D. Weltmann, *J. Phys. D: Appl. Phys.* **2008**, *41*, 194011. https://doi.org/10.1088/0022-3727/41/19/194011
[19] K. McKay, J. S. Oh, J. L. Walsh, J. W. Bradley, *J. Phys. D: Appl. Phys.* **2013**, *46*, 464018. https://doi.org/10.1088/0022-3727/46/46/464018
[20] A. Schmidt-Bleker, J. Winter, S. Iseni, M. Dünnbier, K.-D. Weltmann, S. Reuter, *J. Phys. D: Appl. Phys.* **2014**, *47*, 145201. https://doi.org/10.1088/0022-3727/47/14/145201
[21] D. Riès, G. Dilecce, E. Robert, P. F. Ambrico, S. Dozias, J. M. Pouvesle, *J. Phys. D: Appl. Phys.* **2014**, *47*, 275401. https://doi.org/10.1088/0022-3727/47/27/275401
[22] S. Reuter, J. Winter, A. Schmidt-Bleker, D. Schroeder, H. Lange, N. Knake, V. Schulz-von der Gathen, K. D. Weltmann, *Plasma Sources Sci. Technol.* **2012**, *21*, 024005. https://doi.org/10.1088/0963-0252/21/2/024005
[23] A. Nikiforov, L. Li, N. Britun, R. Snyders, P. Vanraes, C. Leys, *Plasma Sources Sci. Technol.* **2014**, *23*, 015015. https://doi.org/10.1088/0963-0252/23/1/015015
[24] C. Tropea, A. L. Yarin, J. F. Foss, *Springer Handbook of Experimental Fluid Mechanics*, Springer, New York, NY **2007**.
[25] L. Li, A. Nikiforov, Q. Xiong, N. Britun, R. Snyders, X. Lu, C. Leys, *Phys. Plasmas* **2013**, *20*, 093502. https://doi.org/10.1063/1.4820945
[26] S. Yonemori, R. Ono, *J. Phys. D: Appl. Phys.* **2014**, *47*, 125401. https://doi.org/10.1088/0022-3727/47/12/125401
[27] J. Voráč, P. Dvořák, V. Procházka, J. Ehlbeck, S. Reuter, *Plasma Sources Sci. Technol.* **2013**, *22*, 025016. https://doi.org/10.1088/0963-0252/22/2/025016
[28] T. Verreycken, R. M. van der Horst, N. Sadeghi, P. J. Bruggeman, *J. Phys. D: Appl. Phys.* **2013**, *46*, 464004. https://doi.org/10.1088/0022-3727/46/46/464004
[29] G. Dilecce, L. M. Martini, P. Tosi, M. Scotoni, S. De Benedictis, *Plasma Sources Sci. Technol.* **2015**, *24*, 034007. https://doi.org/10.1088/0963-0252/24/3/034007
[30] Y. Yue, X. Pei, X. Lu, *IEEE Trans. Radiat. Plasma Med. Sci.* **2017**, *1*, 6. https://doi.org/10.1109/TRPMS.2017.2757037
[31] R. J. Kee, M. E. Coltrin, P. Glarborg, *Chemically Reacting Flow: Theory and Practice*, Wiley-Interscience, Hoboken, NJ **2003**, https://doi.org/10.1002/0471461296
[32] R. B. Bird, W. E. Stewart, E. N. Lightfoot, *Transport Phenomena*, 2nd edition., John Wiley & Sons, New York, NY **2002**.
[33] S. P. Wasik, K. E. McCulloh, *J. Res. Natl. Bur. Stand.* **1968**, *73A*, 2.
[34] J. H. Rohling, J. Shen, C. Wang, J. Zhou, C. E. Gu, *Appl. Phys. B* **2007**, *87*, 355. https://doi.org/10.1007/s00340-007-2595-9
[35] C. V. Paganelli, F. K. Kurata, *Respir. Physiol.* **1977**, *30*, 15. https://doi.org/10.1016/0034-5687(77)90018-4
[36] T. J. Chung, *Computational Fluid Dynamics*, Cambridge University Press, Cambridge, UK **2002**.
[37] D. Xu, J. Chen, *Exp. Therm. Fluid Sci.* **2013**, *44*, 662. https://doi.org/10.1016/j.expthermflusci.2012.09.006
[38] C. Gualtieri, A. Angeloudis, F. Bombardelli, S. Jha, T. Stoesser, *Fluids* **2017**, *2*, 17. https://doi.org/10.3390/fluids2020017
[39] M. Boselli, V. Colombo, M. Gherardi, R. Laurita, A. Liguori, P. Sanibondi, E. Simoncelli, A. Stancampiano, *IEEE Trans. Plasma Sci.* **2015**, *43*, 3. https://doi.org/10.1109/TPS.2014.2381854
[40] H. Sato, *J. Phys. Soc. Jpn.* **1956**, *11*, 702. https://doi.org/10.1143/JPSJ.11.702
[41] H. Sato, *J. Phys. Soc. Jpn.* **1959**, *14*, 1797. https://doi.org/10.1143/JPSJ.14.1797
[42] E. Gutmark, C.-M. Ho, *Phys. Fluids* **1983**, *26*, 2932. https://doi.org/10.1063/1.864058
[43] J. Cohen, I. Wygnanski, *J. Fluid Mech.* **1987**, *176*, 191. https://doi.org/10.1017/S0022112087000624
[44] S. W. Rienstra, *J. Sound Vib.* **1983**, *86*, 4. https://doi.org/10.1016/0022-460X(83)91019-2
[45] J. Westerweel, C. Fukushima, J. M. Pedersen, J. C. R. Hunt, *Phys. Rev. Lett.* **2005**, *95*, 174501. https://doi.org/10.1103/PhysRevLett.95.174501
[46] B. Lautrup, *Physics of Continuous Matter: Exotic and Everyday Phenomena in the Macroscopic World*, Institute of Physics, Bristol, UK **2005**.
[47] S. Yonemori, Y. Nakagawa, R. Ono, T. Oda, *J. Phys. D: Appl. Phys.* **2012**, *45*, 225202. https://doi.org/10.1088/0022-3727/45/22/225202
[48] T. Murakami, K. Niemi, T. Gans, D. O'Connell, W. G. Graham, *Plasma Sources Sci. Technol.* **2013**, *22*, 015003. https://doi.org/10.1088/0963-0252/22/1/015003

SUPPORTING INFORMATION

Additional supporting information may be found online in the Supporting Information section.

How to cite this article: Morabit Y, Whalley RD, Robert E, Hasan MI, Walsh JL. Turbulence and entrainment in an atmospheric pressure dielectric barrier plasma jet. *Plasma Process Polym.* 2019;e1900217. https://doi.org/10.1002/ppap.201900217